Applied Physics B (2023) 129:140
https://doi.org/10.1007/s00340-023-08082-z

Applied Physics B
Lasers and Optics

RESEARCH

FBG-based 3D shape sensor based on spun multi-core fibre for continuum surgical robots

Kangpeng Zhou[1] · Lianqing Zhu[2,3] · Guangkai Sun[2,3] · Yanlin He[2,3]

Received: 22 May 2023 / Accepted: 26 July 2023 / Published online: 8 August 2023

Abstract

The advance of minimally invasive interventional surgeries has accelerated the iterative upgrading of continuum surgical robots. High compatibility with robotic applications and high precision are key features of sensors for robot navigation. In this paper, a spun multi-core fibre (SMCF) 3D shape sensor for continuum surgical robots is proposed. The sensor is fabricated by ultraviolet (UV) light inscribing fibre Bragg gratings (FBGs) in the SMCF, showing good spectra characteristics. Shape reconstruction is realized by the Frenet–Serret (F–S) frame and sensing characteristics such as twisting, strain and temperature are systematically analyzed. Especially, the twisting characteristics of SMCF and MCF are compared and the feasibility of self-torsional compensation of SMCF is demonstrated. In addition, shape measurement experiments with three known shapes are performed. The mean relative error (MRE) for each shape is 0.49%, 1.90% and 5.13%, respectively. These results show that the proposed sensor can accurately measure 3D shapes with temperature and twisting compensation, enabling its application prospects in the online shape feedback of continuum surgical robots.

1 Introduction

Minimally Invasive Surgeries (MISs) have been widely used clinically because of their benefits of less trauma, fast recovery and strong targeting [1–3]. Different types of surgical robots are qualified to complete surgeries, such as urological, cardiac, thoracic, and hepatobiliary [4–6].

However, conventional surgical robots generally use rigid arms and rotating joints to drive instruments, which have limited degrees of freedom. Improving their flexibility, adaptability, human–computer interaction safety and friendliness, is a challenging task, which restricts the application and development of MISs. To address such problems, continuous surgical robots with infinite degrees of freedom, good flexibility and variable stiffness have attracted the research spotlight.

Continuum robots are flexible and can deform according to the actuator positions, external forces, and environmental constraints. Due to their deformability, shape sensing is a crucial technique for estimating and controlling the curved shape of continuum robots. Moreover, shape sensing enables the robots to achieve the desired position, prevent collisions, or follow a certain path, which is essential for continuum robots navigation [7–9].

Fibre optic sensing (FOS) technology uses optical signals transmitted by fibres to measure pose and force. Its advantages include intrinsic safety, easy integration and anti-electromagnetic interference, which is considered one of the navigation technologies with the greatest application potential [10–12].

✉ Lianqing Zhu
lqzhu_bistu@sina.com

Kangpeng Zhou
fishmore0228@sina.com

Guangkai Sun
guangkai.sun@buaa.edu.cn

Yanlin He
heyanlin@bistu.edu.cn

[1] State Key Laboratory of Precision Measuring Technology and Instruments, Tianjin University, Nankai District, No. 92 Weijin Road, Tianjin 300072, China

[2] Key Laboratory of the Ministry of Education for Optoelectronic Measurement Technology and Instrument, Beijing Information Science and Technology University, Haidian District, No. 12 Xiaoying East Road, QinghеBeijing 100192, China

[3] Beijing Laboratory of Optical Fiber Sensing and System, Beijing Information Science and Technology University, Haidian District, No. 12 Xiaoying East Road, QinghеBeijing 100192, China

In general, an optic fibre is composed of a core and a cladding, with a higher refractive index (RI) in the core than in the cladding. The fibre is made of high-purity silica, with a trace amount of dopants (e.g., SiO_2) to increase the core's refractive index (RI). The properties of germanium-doped silica fiber, such as RI, absorption spectrum, internal stress, density, and nonlinear polarization rate, change permanently when exposed to light at wavelengths, such as blue–green or ultraviolet (UV) light.

At present, a multi-core fibre (MCF), whose core arrangement can well feature the strain relationship in bending, has been used for shape measurement. A fibre Bragg gratings (FBGs)-based array is usually inscribed as the sensing unit into the cores by RI modulation, reflecting corresponding spectra. Wavelength shifts when the fibre is subjected to torsion, tension, bending, and temperature changes. However, attributes, such as the number of sensing points, lengths, and intervals, will introduce large cumulative errors in fibre shape measurement, and it is difficult to achieve high-precision positioning. Floris et al. [13] first reported the method of using SMCF to compensate for twisting. Wolf et al. [14] proposed a method of inscribing FBGs in the SMCF by a femtosecond laser and studied the bending characteristics of the sensor. Bao et al. [15] presented a selective FBG inscription method in a four-core fibre with phase masks. Despite the high volume of research on shape perception, the problem of twisting in shape measurement has not been adequately addressed.

Fibre optic photosensitivity is a physical phenomenon in which the RI of the fibre core changes when the fibre is exposed to a laser with a specific wavelength and intensity. It is a material property that refers to the temporary or permanent change of the physical or chemical properties of a substance under the action of external light. The bandwidth of an FBG depends on the magnitude and length of the RI modulation, that is, the larger the RI modulation, the smaller the bandwidth. [16–18]. Therefore, by controlling the intensity and duration of the laser exposure, the magnitude of the RI modulation induced by fiber photosensitivity can be varied, thus changing the bandwidth of the fiber grating. The grating length of an FBG is usually in the order of millimeters. Its reflectivity is larger than 90%, while its reflection spectral bandwidth is less than 0.3 nm [15, 19]. Smaller reflection bandwidth is conducive to the enhancement of the demodulation accuracy and larger reflectivity is conducive to the improvement of the signal-to-noise ratio. Therefore, the study of highly photosensitive MCF sensor design and its application for shape reconstruction has high value in the field of continuum surgical robot navigation.

In this paper, a high RI quartz and self-torsional structure-based sensor is proposed for shape measurement. The sensor is fabricated by UV light inscribing FBGs into an SMCF. The characteristics of the sensor that are studied include twisting, strain and temperature. Shape measurement experiments with three known shapes are also performed. The main innovations and contributions are: a highly photosensitive multi-core optical fibre sensor based on the spun structure; Effective solution of the twisting problem in 3D measurement, known as the helical angle; Elimination of the cumulative error caused by twisting, which has important application value for improving the navigation accuracy and reducing the positioning error of the continuum surgical robots.

The remainder of this paper is organized as follows. The sensor design and reconstruction method are described in Sect. 2. Experimental results and analysis are presented in Sect. 3. Finally, conclusions are discussed in Sect. 4.

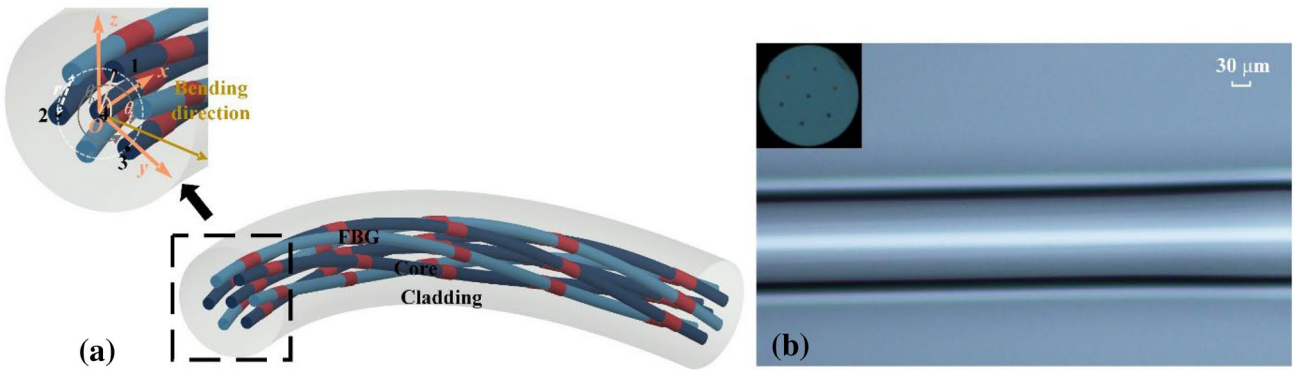

Fig. 1 Structure of the sensor. **a** Schematic diagram and geometric relationship of the SMCF; **b** SMCF micrography

2 Materials and methods

2.1 Sensor design

The structure of the sensor array is shown in Fig. 1. The out cores are designed with a fixed pitch, while the center core is straight. The red parts are the FBGs. The FBGs of each cross section form a node together. A coordinate system centered on the middle core is located on the neutral axis. The cross section is the x-axis and y-axis, and the z-axis is the tangent line along the fibre.

Outer cores, sensitive to bending, are outside the neutral layer. The cores at 120 degrees have good 3D directivity. The dark blue cores (cores numbered 1, 2, 3) in Fig. 1 are selected as the sensing source for shape measurement.

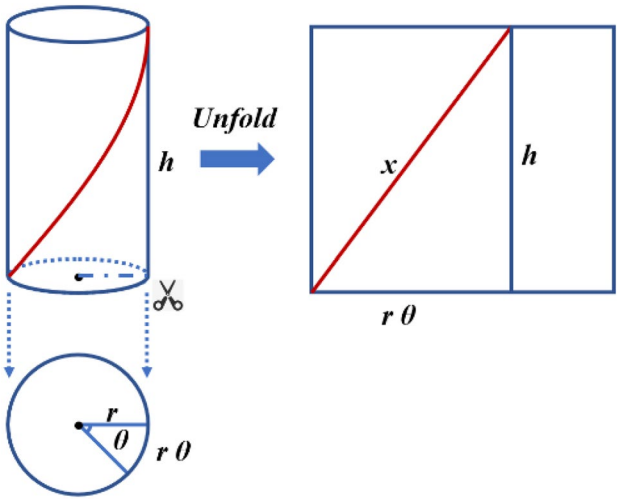

Fig. 2 Geometric relationship of the MCF

2.2 Sensing model

For each FBG, the Bragg wavelength λ_B is defined as [8]

$$\lambda_B = 2n_{eff}\Lambda, \tag{1}$$

where n_{eff} is the core effective RI and Λ is the grating period. For strain ($\Delta\varepsilon$) and temperature (ΔT)-induced wavelength shift $\Delta\lambda$, Eq. (1) can be converted to

$$\frac{\Delta\lambda}{\lambda_B} = [(1-P_\varepsilon)\cdot\Delta\varepsilon + (\alpha+\varsigma)\cdot\Delta T] = k_\varepsilon\Delta\varepsilon + k_T\Delta T, \tag{2}$$

where P_ε is the photoelastic coefficient, α is the thermal expansion coefficient, ς is the thermal optical coefficient, k_ε is the strain sensitivity coefficient and k_T is the temperature sensitivity coefficient. Therefore, core–strain relation equations can be expressed as [20]

$$\begin{cases} \varepsilon_1 = -kr\cos\left(\theta_b - \frac{3}{2}\pi - \theta_1\right) + \varepsilon_4 \\ \varepsilon_2 = -kr\cos\left(\theta_b - \frac{3}{2}\pi - \theta_2\right) + \varepsilon_4 \\ \varepsilon_3 = -kr\cos\left(\theta_b - \frac{3}{2}\pi - \theta_3\right) + \varepsilon_4 \end{cases} \tag{3}$$

where $\varepsilon_i(1,2,3)$ is the strain, k is the curvature, r is the core spacing, θ_b is the bending angle and ε_4 is measured by the center core (No. 4) with axial bias induced by applied strain, temperature variation and spectral fluctuation.

The cores of the SMCF have their own helix and constant pitch. Assuming that the fibre is a cylinder (Fig. 2), if it is sheared along its normal line, the geometric relationship between the length of the core (x), the pitch (h) and core spacing (r) is [21]

$$x = \sqrt{h^2 + r^2\theta^2}, \tag{4}$$

where θ is the torsion angle. Torsion ε_τ can be expressed as

$$\varepsilon_\tau = \frac{x-h}{h} = \frac{\sqrt{h^2 + r^2\theta^2} - h}{h}. \tag{5}$$

Finally, the torsion angle $\theta = \pm\sqrt{\frac{h^2\varepsilon_\tau^2 + 2h^2\varepsilon_\tau}{r^2}}$.

2.3 3D shape reconstruction frame

Shape reconstruction is realized by the Frenet–Serret (F–S) frame. The Frenet frame is composed of the tangent vector T, the normal vector N, and the subnormal vector B. The three vectors form a set of orthonormal basis, which can be used to describe the position of any point on the space curve r (s). To describe the change law of the curvature torsion of the space curve, the derivative of the three vectors with the curve can be expressed as [20]

$$\frac{d}{ds}\begin{pmatrix} T(s) \\ N(s) \\ B(s) \end{pmatrix} = \begin{pmatrix} 0 & k(s) & 0 \\ -k(s) & 0 & \tau(s) \\ 0 & -\tau(s) & 0 \end{pmatrix}\begin{pmatrix} T(s) \\ N(s) \\ B(s) \end{pmatrix}. \tag{6}$$

For calculating the coordinates of the discrete points of the space curve, an eigenmatrix X (s) is introduced, which can be expressed as

$$\begin{aligned} &\frac{d}{ds}X(s) = X(s)A(s) \\ &= \begin{bmatrix} T(s) & N(s) & B(s) & r(s) \\ 0 & 0 & 0 & 1 \end{bmatrix}\begin{bmatrix} 0 & -k(s) & 0 & 1 \\ k(s) & 0 & -\tau(s) & 0 \\ 0 & 0 & 0 & 0 \\ 0 & 0 & 0 & 0 \end{bmatrix}, \end{aligned} \tag{7}$$

where $A(s)$ represents the position information of the current point. After each iteration, the curve can be completely delineated. Taken as an integral, Eq. (7) can be expressed as

$$\int X(s)ds = e^{A(s)s}. \tag{8}$$

Finally, curve coordinates including point spacing Δs can be expressed as

$$X(s+\Delta s) = X(s)e^{(A(s)\Delta s)}. \tag{9}$$

3 Experimental results and analysis

3.1 Sensor fabrication and spectral analysis

The FBG inscribing system setup is shown in Fig. 3. It includes an optical module and a monitoring and control system. The FBGs are fabricated by UV light (248 nm, Coherent Co.) exposure with phase masks, whose ± 1 order diffraction light forms interference fringes on the fibre (SSM-7C1500(6.1/125)/002) to realize RI modulation. The monitoring and control system comprises an FBG interrogator (Xufeng Photoelectric Co.), a fan out unit (Fibrecore Co.) and a computer.

First, the fibre was hydrogen loaded to ensure the FBG can be inscribed. Then, 6 mm-long FBGs were inscribed in each core, with a spacing of 20 mm between adjacent FBGs, forming a four-node sensor array. Spectra are shown in Fig. 4. The reflectivity of FBG is related to the grating length and RI modulation depth. Simultaneously, RI modulation depth and longer gratings have higher reflectivity. In addition, arrays of short grating lengths will enhance reconstruction accuracy. As a result, it is highly important and valuable to the research of SMC–FBGs.

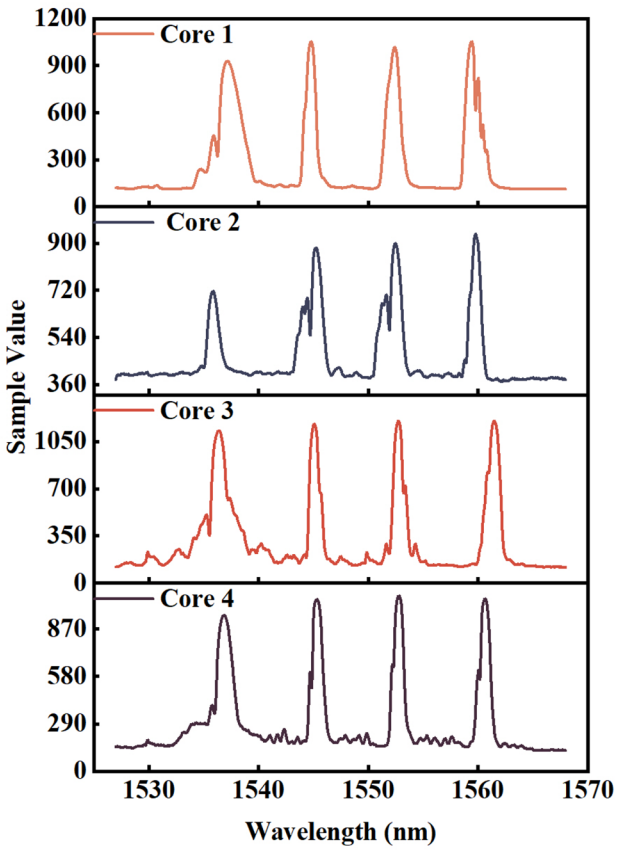

Fig. 4 Spectra of FBGs inscribed into SMCF

3.2 Sensing characteristics analysis

The experimental system setup for sensing characteristics analysis is shown in Fig. 5. Twisting, strain, and temperature are tested in the experiment.

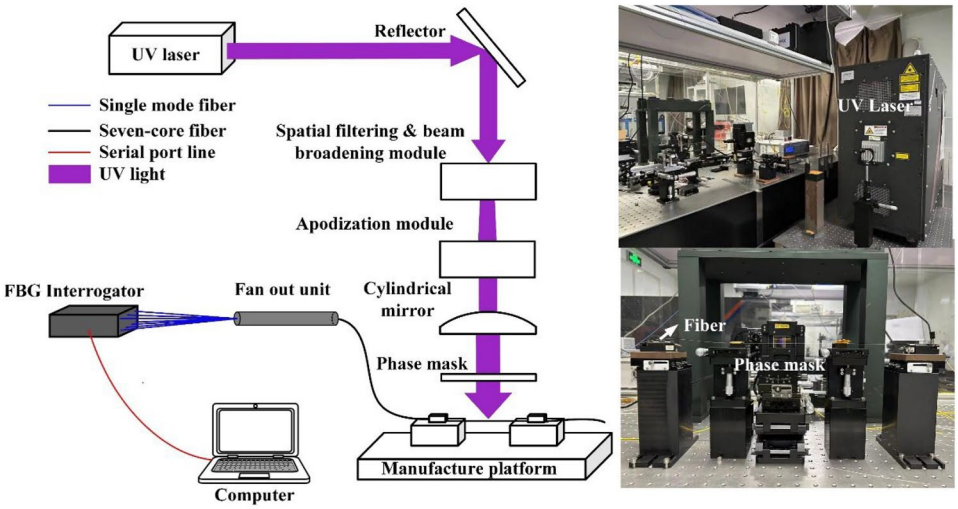

Fig. 3 MCF–FBG inscribing system

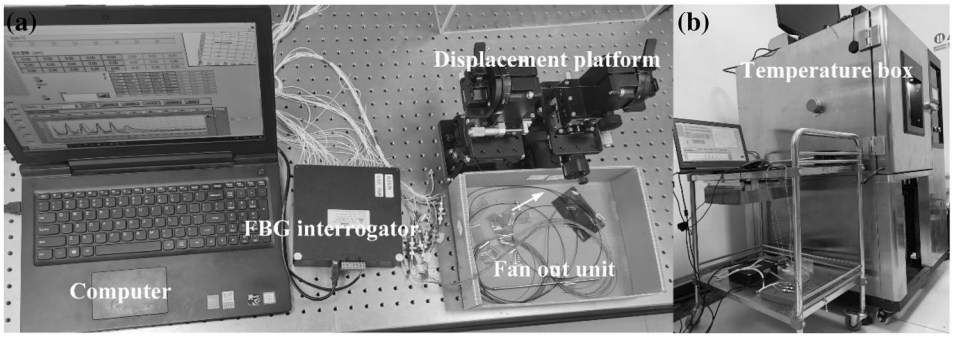

Fig. 5 Experimental system setup. **a** Strain and twisting test system; **b** temperature test system

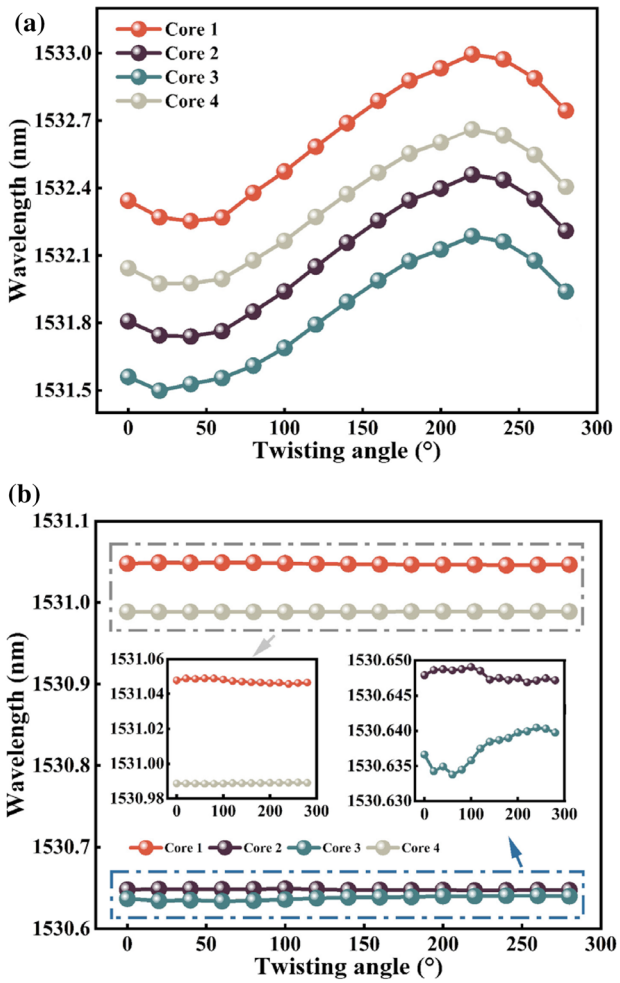

Fig. 6 Wavelength–angle fitting curves. **a** SMCF; **b** MCF

3.2.1 Twisting measurement

Twisting tests are performed on the two types of fibre, respectively (Fig. 5a). The sensors are fixed by a 3D precise displacement platform, which can stretch and spin. The wavelength–angle relation curves are obtained with twisting angles ranging from 0° to 280° and sampling at an interval of 20°.

Figure 6a shows the wavelength–angle fitting curves of the spun fibre array. Cores' numbers correspond to the number in Fig. 1. Sine functions are used to fit the discrete points. The equations fitting to the four curves can be expressed as

$$\begin{cases} \lambda_1 = 0.3540 \sin\left[\frac{(\alpha_1 - 127.1980)\pi}{179.9494}\right] + 1532.6157 \\ \lambda_2 = 0.3461 \sin\left[\frac{(\alpha_2 - 126.7899)\pi}{180.9302}\right] + 1532.0581 \\ \lambda_3 = 0.3223 \sin\left[\frac{(\alpha_3 - 126.2453)\pi}{182.0656}\right] + 1531.8300 \\ \lambda_4 = 0.3301 \sin\left[\frac{(\alpha_4 - 126.3719)\pi}{178.4724}\right] + 1532.3026 \end{cases}, \quad (10)$$

where $\alpha_i (i = 1, 2, 3, 4)$ are the twisting angles and $\lambda_i (i = 1, 2, 3, 4)$ the wavelengths. All the cores exhibit the same trend, indicating the magnitude and direction of

Table 1 Strain sensitivity values on average

Cores	Nodes (pm/με)			
	1	2	3	4
1	0.89	0.87	0.90	0.91
2	0.88	0.88	0.89	0.90
3	0.88	0.87	0.89	0.90
4	0.88	0.87	0.90	0.91
Average value	0.88	0.88	0.90	0.91

Table 2 Temperature sensitivity values on average

Cores	Nodes (pm/ºC)			
	1	2	3	4
1	9.93	9.93	9.90	10.07
2	9.98	9.28	10.03	9.97
3	9.95	9.72	9.91	10.01
4	9.82	10.72	9.83	10.13
Average value	9.92	9.91	9.92	10.04

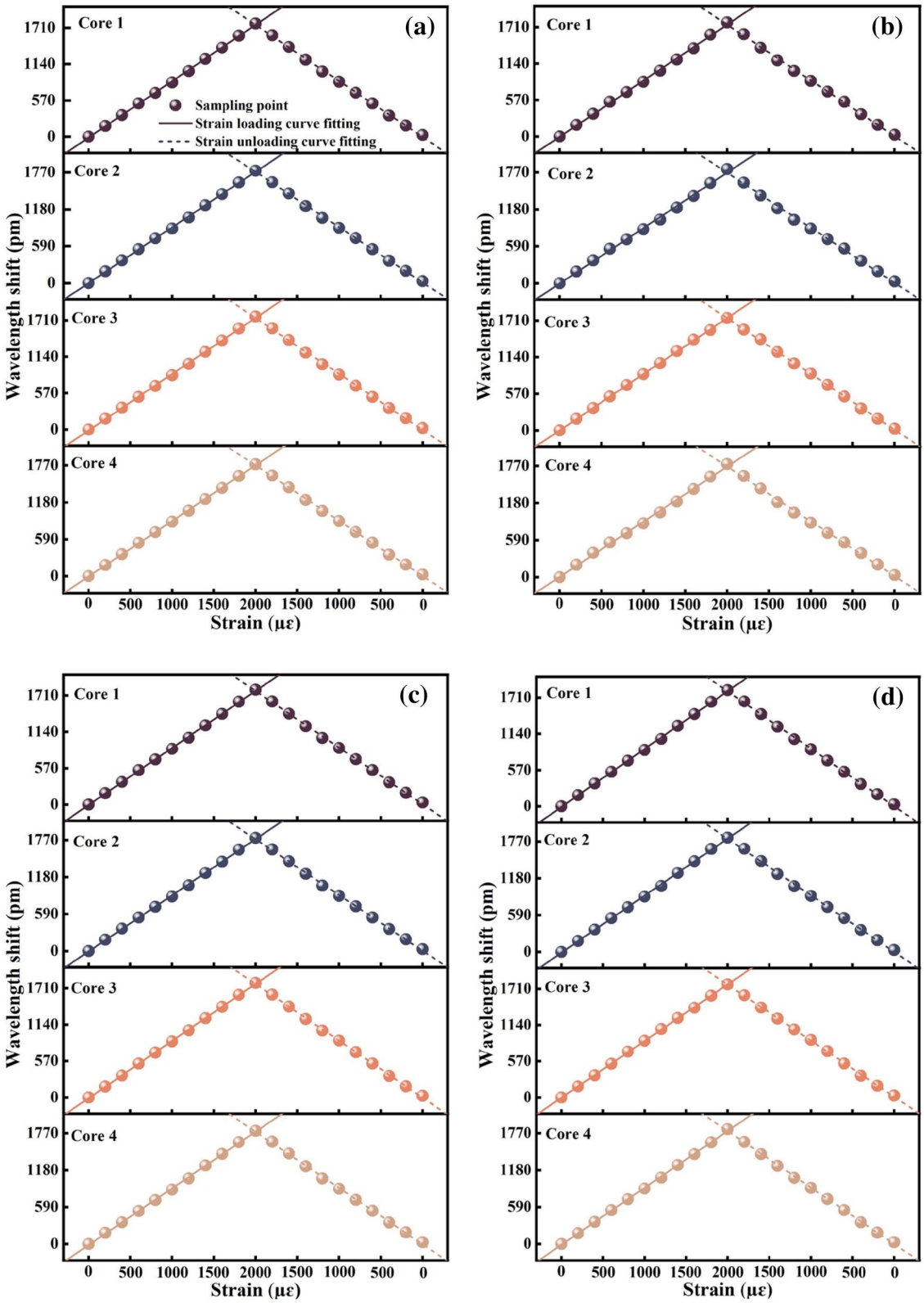

Fig. 7 Strain fitting curves. **a** Node 1; **b** Node 2; **c** Node 3; **d** Node 4

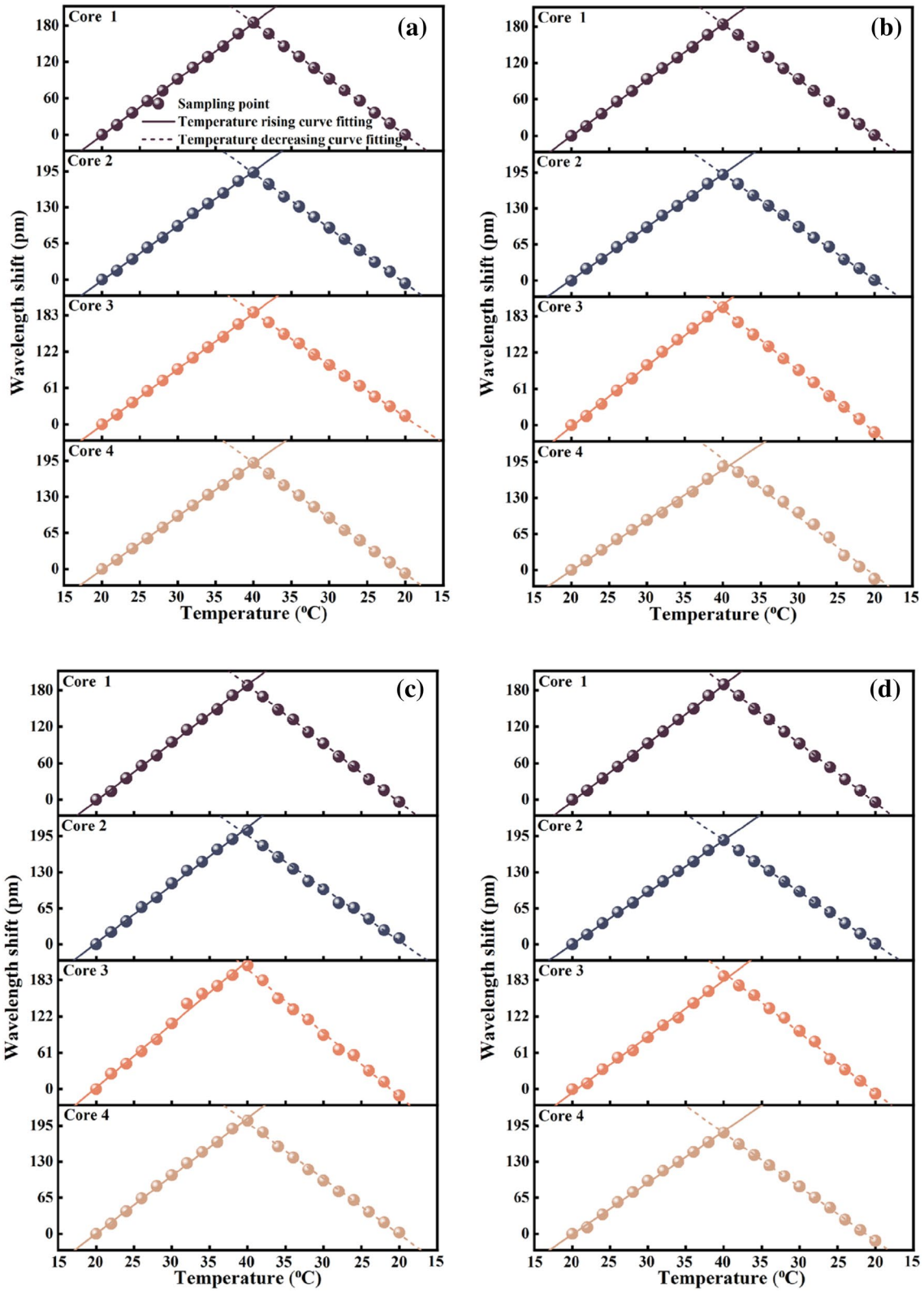

Fig. 8 Temperature fitting curves. **a** Node 1; **b** Node 2; **c** Node 3; **d** Node 4

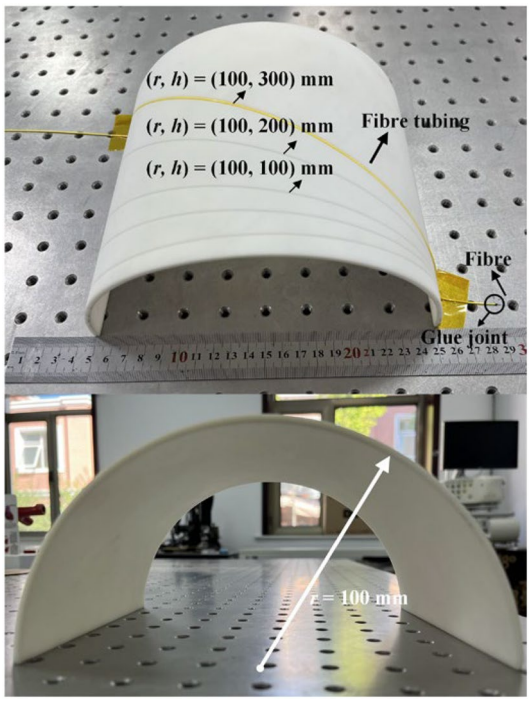

Fig. 9 3D shape measurement experiment

torsion. The twist sensitivity is 0.12 pm/° with an accuracy of 3.14°. Results show that in shape measurement, the centre core can be used as the reference for twisting-strain decoupling. Compared with Fig. 6a, the results of the parallel fibre shown in Fig. 6b are irregular, and the results of the cores trend are also inconsistent. In other words, in 3D shape measurement, the error caused by torsion cannot be ignored.

3.2.2 Strain/temperature sensitivity calibration

The strain introduced to the fibre is calculated by rotating the highly precise micrometer of the displacement platform to adjust the distance. The maximum strain is set as 0–2000 με with sampling points at an interval of 200 με, which covers the range of bending strain variation for shape reconstruction. The experiment includes the loading and unloading strain process and is repeated three times and each obtained FBG sensitivity value is averaged. Results are shown in Table 1 and Fig. 7. All the sensitivity values are close, and the average value is 0.89 pm/με with an accuracy of 118.44 με.

For the temperature sensitivity calibration, the sensor is placed into the temperature box (GDW-100, 0.1 °C @ (− 70 ~ 160) °C) (Fig. 5b). The experimental temperature range is 20–40 °C at an interval of 2 °C, which simulates the temperature change during the surgical procedure. Similar to the strain sensitivity calibration, three sets of increasing and decreasing the temperature are performed. The average results

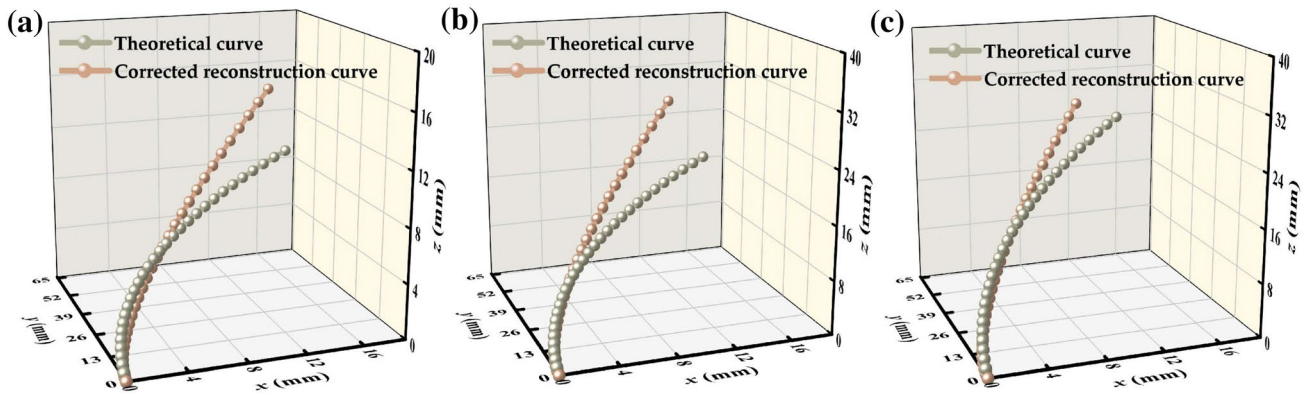

Fig. 10 Reconstruction results. **a** $r = 100$ mm, $h = 100$ mm; **b** $r = 100$ mm, $h = 200$ mm; **c** $r = 100$ mm, $h = 300$ mm

Table 3 Node errors of the reconstruction curves

No	Shapes (r, h, mm)	Nodes relative error				MRE
		1	2	3	4	
1	$r = 100$, $h = 100$	/	0.41%	0.05%	0.75%	0.49%
2	$r = 100$, $h = 200$	/	1.73%	0.36%	2.36%	1.90%
3	$r = 100$, $h = 300$	/	6.59%	2.02%	1.31%	5.13%

are shown in Table 2 and Fig. 8. The FBGs on each node have a certain deviation varied from 9.28 pm/°C to 10.72 pm/°C, and the maximum bias is 1.44 pm with an accuracy of 0.68 °C. According to Eq. (2), a drift of 1 pm causes a deviation of 0.1 °C, so the average temperature sensitivity of 9.95 pm/°C can be applied to the follow-up experiments.

3.2.3 Shape reconstruction

A 3D-printed standard plate (Fig. 9) with known shapes is used in the shape measurement experiment. First, the fibre was protected by a fibre tubing (FT900Y, Thorlabs Co.) and spot-glued to it on one side to avoid continuous strain distribution in the sensor array during the experiment. Then, the sensor array was placed in the grooves with shapes of (r, h) (unit: mm) = (100,100), (100,200), and (100,300), where r was the radius and h was the pitch.

In shape reconstruction, we collected and averaged 1000 sets of data for each shape. We used the bending-insensitive centre core (1) on the neutral layer to calibrate the strain values of the outer cores (1, 2, 3) FBGs with Eq. (1) and Eq. (2). The cubic splines method were applied for the strain interpolation between two adjacent nodes. Finally, the calibrated curve were obtained. The reconstruction results are shown in Fig. 10.

Reconstruction errors are evaluated by comparing the node-origin distance. δ is substituted to describe the reconstruction error, which can be defined as

$$\delta = \sqrt{\frac{(x_m - x_t)^2 + (y_m - y_t)^2 + (z_m - z_t)^2}{x_t^2 + y_t^2 + z_t^2}} \times 100\% \qquad (11)$$

where (x_m, y_m, z_m) is the measured coordinate and (x_t, y_t, z_t) is the theoretical coordinate. The relative error of the nodes is shown in Table 3. As the pitch h increases, the mean relative error (MRE) also increases for each shape, reaching 0.49%, 1.90% and 5.13%, respectively.

4 Conclusion

In this paper, a fibre Bragg grating (FBG) shape sensor is proposed based on photo-sensitively structural spun multi-core fibre (SMCF). The fibre used in the sensor fabrication shows high photosensitivity, and FBGs with better spectral characteristics can be easily created. The twisting characteristics of SMCF and MCF are compared and the feasibility of self-torsional compensation of SMCF is proved. Strain and temperature sensitivities are calibrated. Finally, three shape reconstruction by Frenet–Serret (F–S) frame is realized. The mean relative error (MRE) for each shape is 0.49%, 1.90% and 5.13%, respectively. The work conducted in this paper provides a novel approach for shape measurement with twisting self-compensation. The proposed sensor has application prospects in improving the navigation accuracy and reducing positioning errors of continuum surgical robots.

Acknowledgements This work was supported by the Key Project of Beijing Municipal Education Commission Science and Technology Program (No. KZ201911232044), the Beijing Nova Program of Science and Technology (No. Z191100001119052), the National Key Research and Development Program of China (No. 2020YFA0711200) and the National Natural Science Foundation of China (No. 52275517).

Author contributions Investigation, K.Z; Methodology, K.Z., G.S.; Writing - original draft, K.Z; Supervision, L.Z.; Writing – review & editing, G.S, Y.H, and L.Z.; Software, K.Z. All authors have read and agreed to the published version of the manuscript.

Funding Funding was provided by the Key Project of Beijing Municipal Education Commission Science and Technology Program (No. KZ201911232044), the Beijing Nova Program of Science and Technology (No. Z191100001119052), the National Key Research and Development Program of China (No. 2020YFA0711200) and the National Natural Science Foundation of China (No. 52275517).

Declarations

Competing interests The authors declare no competing interests.

References

1. Y. Lu, B. Lu, B. Li, H. Guo, Y.H. Liu, IEEE Robot Autom Lett **6**, 4835 (2021)
2. X.T. Ha, M. Ourak, O. Al-Ahmad, D. Wu, G. Borghesan, A. Menciassi, and E. Vander Poorten, IEEE Sens J **21**, 23422 (2021)
3. R. Zhang, H. Liu, and J. Han, Proceedings of the Annual International Conference of the IEEE Engineering in Medicine and Biology Society, EMBS 925 (2017).
4. S. Sefati, R. Hegeman, F. Alambeigi, I. Iordachita, P. Kazanzides, H. Khanuja, R. H. Taylor, and M. Armand, IEEE/ASME Transactions on Mechatronics **26**, 369–380 (2021).
5. R. Xu, A. Yurkewich, R.V. Patel, IEEE Robot Autom Lett **1**, 1052 (2016)
6. F. Qi, B. Chen, S. She, S. Gao, Ind. Robot. **48**, 259 (2020)
7. J. Li, F. Zhang, H. Liu, J. Li, F. Zhang, H. Liu, J. Li, F. Zhang, H. Liu, J. Li, Z. Yang, Z. Jiang, IEEE Robot Autom Lett **7**, 3130 (2022)
8. Y. Chitalia, N.J. Deaton, S. Jeong, N. Rahman, J.P. Desai, IEEE Robot Autom Lett **5**, 1712 (2020)
9. V. Modes, T. Ortmaier, J. Burgner-Kahrs, IEEE Sens J **21**, 6712 (2021)
10. P. Jiao, Y. Xie, S. Wu, X. Liu, Materials **13**, 2599 (2020)
11. Z. Liu, S. Lu, D. Wang, Y. Guo, and L. Wu, Materials **15**, (2022).
12. V. Vekteris, M. Jurevicius, V. Turla, Appl Phys B **121**, 203 (2015)
13. I. Floris, J. Madrigal, S. Sales, P. A. Calderón, and J. M. Adam, Mech Syst Signal Process **140**, (2020).
14. A. Wolf, K. Bronnikov, S. Yakushin, A. Dostovalov, S. Zhuravlev, al Alexey Wolf, M. Salganskii, O. Egorova, S. Semjonov, and S. Babin, Seventh European Workshop on Optical Fibre Sensors (EWOFS 2019) **11199**, 475 (2019).
15. W. Bao, N. Sahoo, Z. Sun, C. Wang, S. Liu, Y. Wang, and L. Zhang, Opt Express **28**, (2020).

16. A. Halstuch and A. A. Ishaaya, Opt Lasers Eng **160**, (2023).
17. R. Idrisov, A. Lorenz, M. Rothhardt, and H. Bartelt, Sensors **22**, (2022).
18. R. Mahakud, J. Kumar, O. Prakash, S.K. Dixit, S.V. Nakhe, Appl Phys B **121**, 283 (2015)
19. J. Xin, W. Zhuang, X. Lou, L. Zhu, M. Dong, Opt. Eng. **58**, 1 (2019)
20. F. Khan, A. Denasi, D. Barrera, J. Madrigal, S. Sales, S. Misra, IEEE Sens J **19**, 5878 (2019)
21. T. Li, C. Shi, Y. Tan, and Z. Zhou, IEEE Sens J **17**, (2017).